

# Measurements of HNO<sub>3</sub> and N<sub>2</sub>O<sub>5</sub> using ion drift-chemical ionization mass spectrometry during the MILAGRO/MCMA-2006 campaign

J. Zheng<sup>1</sup>, R. Zhang<sup>1</sup>, E. C. Fortner<sup>1,\*</sup>, R. M. Volkamer<sup>2,3</sup>, L. Molina<sup>2</sup>, A. C. Aiken<sup>3,4</sup>, J. L. Jimenez<sup>3,4</sup>, K. Gaeggeler<sup>5</sup>, J. Dommen<sup>5</sup>, S. Dusanter<sup>6</sup>, P. S. Stevens<sup>6</sup>, and X. Tie<sup>7</sup>

<sup>1</sup>Dept. of Atmospheric Sciences, Texas A&M University, College Station, Texas 77843, USA

<sup>2</sup>Molina Center for Energy and the Environment, La Jolla, California and Massachusetts Institute of Technology, Cambridge, Massachusetts, USA

<sup>3</sup>Dept. of Chemistry and Biochemistry, University of Colorado at Boulder, Boulder CO, USA

<sup>4</sup>Cooperative Institute for Research in the Environmental Sciences (CIRES), University of Colorado, Boulder, Colorado, USA

<sup>5</sup>Laboratory of Atmospheric Chemistry, Paul Scherrer Institute, Switzerland

<sup>6</sup>Dept. of Chemistry, Indiana University, Bloomington, Indiana, USA

<sup>7</sup>Atmospheric Chemistry Division, National Center for Atmospheric Research, Boulder, Colorado, USA

\*now at: Dept. of Chemistry and Biochemistry, Montana State University, Bozeman, Montana, USA

Received: 18 January 2008 – Published in Atmos. Chem. Phys. Discuss.: 6 March 2008

Revised: 1 September 2008 – Accepted: 7 October 2008 – Published: 28 November 2008

**Abstract.** An ion drift-chemical ionization mass spectrometer (ID-CIMS) was deployed in Mexico City between 7 and 31 March to measure gas-phase nitric acid (HNO<sub>3</sub>) and dinitrogen pentoxide (N<sub>2</sub>O<sub>5</sub>) during the Mexico City Metropolitan Area (MCMA)-2006 field campaign. The observation site was located at the Instituto Mexicano del Petróleo in the northern part of Mexico City urban area with major emissions of pollutants from residential, vehicular and industrial sources. Diurnally, HNO<sub>3</sub> was less than 200 parts per trillion (ppt) during the night and early morning. The concentration of HNO<sub>3</sub> increased steadily from around 09:00 a.m. central standard time (CST), reached a peak value of 0.5 to 3 parts per billion (ppb) in the early afternoon, and then declined sharply to less than half of the peak value near 05:00 p.m. CST. An inter-comparison between the ID-CIMS and an ion chromatograph/mass spectrometer (ICMS) showed a good agreement between the two HNO<sub>3</sub> measurements ( $R^2=0.75$ ). The HNO<sub>3</sub> mixing ratio was found to anti-correlate with submicron-sized aerosol nitrate, suggesting that the gas-particle partitioning process was a major factor in determining the gaseous HNO<sub>3</sub> concentration. Losses by irreversible

reactions with mineral dust and via dry deposition also could be important at this site. Most of the times during the MCMA 2006 field campaign, N<sub>2</sub>O<sub>5</sub> was found to be below the detection limit (about 30 ppt for a 10 s integration time) of the ID-CIMS, because of high NO mixing ratio at the surface (>100 ppb) during the night. An exception occurred on 26 March 2006, when about 40 ppt N<sub>2</sub>O<sub>5</sub> was observed during the late afternoon and early evening hours under cloudy conditions before the build-up of NO at the surface site. The results revealed that during the MCMA-2006 field campaign HNO<sub>3</sub> was primarily produced from the reaction of OH with NO<sub>2</sub> and regulated by gas/particle transfer and dry deposition. The production of HNO<sub>3</sub> from N<sub>2</sub>O<sub>5</sub> hydrolysis during the nighttime was small because of high NO and low O<sub>3</sub> concentrations near the surface.

## 1 Introduction

For decades, the Mexico City Metropolitan Area (MCMA), one of the largest megacities in the world, has suffered from poor air quality, particularly high concentrations of ozone (O<sub>3</sub>) and particulate matter (Molina and Molina, 2002; Molina et al., 2007). As the home of about 20 million residents, over 4 million vehicles, and more than 45 000



Correspondence to: R. Zhang  
(zhang@ariel.met.tamu.edu)

industries, the MCMA emits annually near 180 kilotons ( $10^3$  metric tons) of nitrogen oxides ( $\text{NO}_x = \text{NO} + \text{NO}_2$ ), 6.7 kilotons of sulfur dioxide ( $\text{SO}_2$ ), and 532 kilotons of volatile organic compounds (VOCs) into the atmosphere (CAM, 2006). Furthermore, the unique combination of geographical conditions, i.e., a basin topography, intense tropical solar radiation ( $19^{\circ}25' \text{N}$  and  $99^{\circ}10' \text{W}$ ), and high elevation (2240 m above mean sea level), makes air pollutants easier to accumulate in the MCMA and is favorable for photochemical production of  $\text{O}_3$  and aerosols (Molina and Molina, 2002; Zhang et al., 2004a; Salcedo et al., 2006; Volkamer et al., 2006). During the late 1980s and early 1990s, this region annually experienced an hourly average  $\text{O}_3$  concentration higher than 110 ppb on over 80% of days and the peak  $\text{O}_3$  concentration exceeded 300 ppb on over 10% of days (Molina and Molina, 2002). The air quality has improved significantly recently due to control strategies implemented by the Mexican government authorities (Molina and Molina, 2004; Molina et al., 2008).

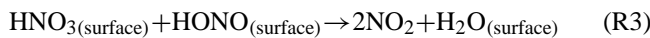
During the MCMA-2006 field study, a component of the MILAGRO Campaign (Molina et al., 2008), daytime  $\text{O}_3$  at the urban site was frequently higher than 100 ppb and decreased to a few ppb at night due to a large amount of fresh  $\text{NO}_x$  emissions, resulting in a daily average  $\text{NO}_x$  concentration of over 100 ppb. Both VOCs and  $\text{NO}_x$  play critical roles in the  $\text{O}_3$  formation in the troposphere (Finlayson-Pitts and Pitts, 1999; Tie et al., 2001; Zhang et al., 2003). Depending on the concentrations of VOCs and  $\text{NO}_x$ ,  $\text{O}_3$  production rate can be either  $\text{NO}_x$ -sensitive or VOC-sensitive (Sillman, 1999; Lei et al., 2004; Zhang et al., 2004b). Recent chemical transport model simulations suggested that the  $\text{O}_3$  formation in the MCMA was VOC-limited (Lei et al., 2007; Tie et al., 2007). The lifecycle of  $\text{NO}_x$  and its budget in the MCMA represents one of the critical pieces of information that is required to develop effective  $\text{O}_3$  control strategies (Lei et al., 2007). The dominant daytime sink of  $\text{NO}_x$  is through the oxidation of  $\text{NO}_2$  by the hydroxyl radical ( $\text{OH}$ ) to form nitric acid ( $\text{HNO}_3$ ).



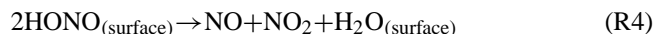
Nitric acid is removed from the atmosphere by dry and wet depositions (Finlayson-Pitts and Pitts, 1999). Generally,  $\text{HNO}_3$  deposition is considered to be an irreversible sink of  $\text{NO}_x$ , but recent studies have suggested that  $\text{HNO}_3$  deposited on the surface can be recycled back into the atmosphere as  $\text{NO}_x$  by heterogeneous reactions with NO. For example, Saliba et al. (2001) proposed that  $\text{HNO}_3$  on the surface reacts with NO to form  $\text{NO}_2$  and nitrous acid (HONO).



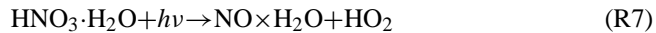
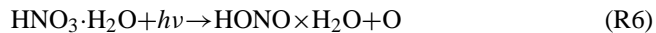
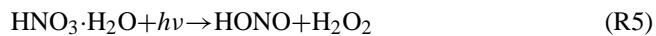
Further reaction between HONO and  $\text{HNO}_3$  forms  $\text{NO}_2$



or between two HONO molecules forms NO and  $\text{NO}_2$ ,



Moreover, Ramazan et al. (2006) suggested that  $\text{HNO}_3 \cdot \text{H}_2\text{O}$  complex could be photolyzed, forming HONO or NO.



Thus, under certain meteorological conditions, a  $\text{HNO}_3$  enriched plume can potentially contribute to  $\text{O}_3$  production far away from its origin.

At nighttime,  $\text{NO}_x$  reacts with  $\text{O}_3$  to form the nitrate radical ( $\text{NO}_3$ ), which further reacts reversibly with  $\text{NO}_2$  to form dinitrogen pentoxide ( $\text{N}_2\text{O}_5$ ) (for Reaction 10,  $K_{\text{eq}} = 2.7 \times 10^{-27} \exp[11000/T] \text{ cm}^3 \text{ molecule}^{-1}$ , JPL 2006).



At night,  $\text{NO}_3$  can exist in significant concentrations and initiate H-atom abstraction or addition reactions with hydrocarbons in a similar way as OH radicals during daytime (Suh et al., 2001). Compared to  $\text{NO}_3$ ,  $\text{N}_2\text{O}_5$  is relatively unreactive in the gas-phase but undergoes heterogeneous hydrolysis reaction to form  $\text{HNO}_3$  (Zhang et al., 1995; Brown et al., 2006).



Recent laboratory studies also suggested that  $\text{NO}_3$  and  $\text{N}_2\text{O}_5$  could also react with soot to produce  $\text{NO}_x$ , providing another possible pathway of renoxification (Karagulian and Rossi, 2007). Therefore, in situ observations of  $\text{HNO}_3$  and  $\text{N}_2\text{O}_5$  are important to fully characterize the  $\text{NO}_x$  chemistry and budget in the troposphere and to develop effective control strategies.

Several analytical techniques have been developed to measure gaseous  $\text{HNO}_3$  in the troposphere, including nylon filter (Anlauf et al., 1988), mist chamber (Talbot et al., 1990), denuder technique (Perrino et al., 1990; Simon et al., 1995), luminol method (Hering et al., 1988), tunable diode laser spectroscopy (Horii et al., 2006), and chemical ionization mass spectrometry (CIMS) (Huey et al., 1998). Among the different approaches, the CIMS technique has the advantages of high sensitivity and fast time-response (Huey, 2007). The ion drift-chemical ionization mass spectrometry (ID-CIMS) (Fortner et al., 2004) has several additional advantages compared to the traditional CIMS technique. First,

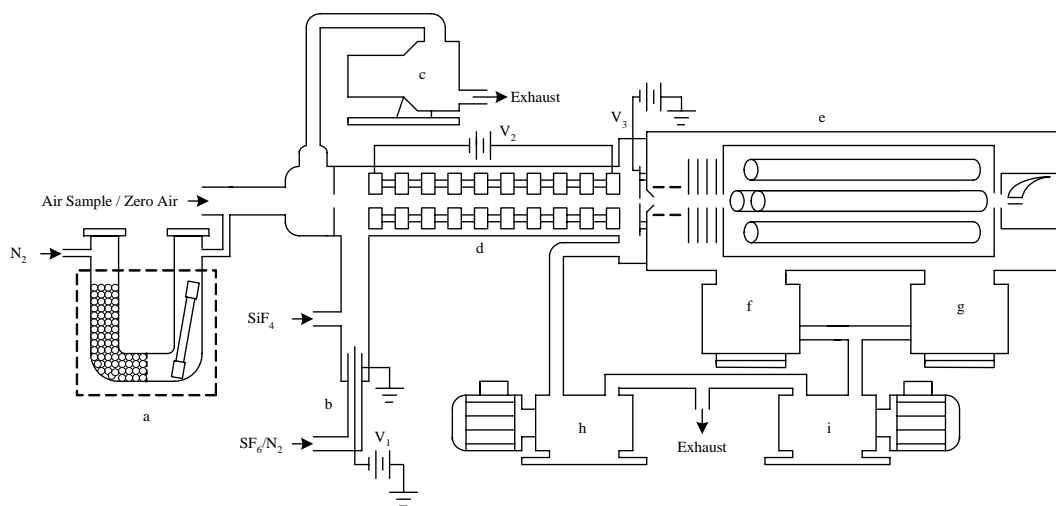


**Fig. 1.** Schematic diagram of the ID-CIMS: (a),  $\text{HNO}_3$  permeation device; (b), ion source; (c), dry scroll pump for air sampling; (d), 10-ring drift tube; (e), Extrel 150-QC mass spectrometer; (f) and (g), Varian VT-551 turbo pumps; (h), Edwards E2M30 oil pump; (i), Varian DS402 oil pump.

a drift tube acts as ion optics (Einzel lens) to focus ions and improves the instrument sensitivity. Second, the electric field inside the drift tube guides the ion trajectory and controls the ion-molecule reaction time so that species can be quantified through kinetic calculations. Third, the presence of an appropriate electric field can inhibit formation of ion clusters inside the drift tube by collisions with carrier gas molecules.

The ambient  $\text{HNO}_3$  mixing ratio varies considerably temporally and spatially, with reported values ranging from a few tens of ppt in clean remote environment to tens of ppb in aged urban plumes (Furutani and Akimoto, 2002; Huey et al., 2004). Despite the importance of  $\text{N}_2\text{O}_5$  in the nocturnal  $\text{NO}_x$  chemistry, in situ  $\text{N}_2\text{O}_5$  measurements have become possible only recently. Measurements of  $\text{N}_2\text{O}_5$  have been performed by using cavity ring-down spectroscopy (CRDS) (Brown et al., 2002) and the CIMS technique (Huey et al., 1995). The measured  $\text{N}_2\text{O}_5$  concentrations range from a few ppt to several hundreds of ppt (Brown et al., 2001; 2006; Slusher et al., 2004).

A series of field campaigns have been conducted in the Mexico City Metropolitan Area, such as the MCMA 2002, 2003 and 2006 field campaigns (Molina et al., 2007; Molina et al., 2008). The objectives of these campaigns are to fully characterize and update the emissions, to investigate the underlying chemical processes that are responsible for secondary air pollutant formation and to facilitate the development of cost-effective control strategies. In this paper, we present measurements of  $\text{HNO}_3$  and  $\text{N}_2\text{O}_5$  during the MCMA 2006 campaign using the ID-CIMS technique for its first field deployment. The results provide insights into the production and gas/particle partitioning of  $\text{HNO}_3$  in MCMA.

## 2 Experimental

### 2.1 ID-CIMS

The ID-CIMS method has been previously described (Fortner et al., 2004), and only details pertinent to this work are provided. Figure 1 shows a schematic diagram of the ID-CIMS that consists of an ion-drift tube, an ion source, and a quadrupole mass spectrometer. Also depicted in Fig. 1 is the  $\text{HNO}_3$  calibration device, which consists of a U-shape 2.54 cm outer diameter (OD) and 17.8 cm long glass tube wrapped with a temperature-regulated heating jacket (the dashed line in Fig. 1). The U-tube has two symmetrical compartments divided by a glass grid in the middle, with one housing a 5.0 cm long Teflon permeation tube (VICI Metronics Inc.) and the other filled with 0.5 cm diameter glass beads to heat the carrier gas uniformly. A corona discharge is used to produce the ions; it consists of a stainless steel needle biased by about  $-1200$  volts ( $V_1$ ) and a grounded 0.6 cm OD stainless steel tubing. A dry scroll pump (Varian) with a 500 standard liter per minute (slpm) pumping speed draws the ambient air into the ID-CIMS system. A small portion of the air is introduced into the drift tube region through an orifice of about 0.5 mm. Within the drift tube, the reagent ions are produced and the ion-molecule reaction occurs to ionize the neutral analyte species. The ion-drift tube is pumped by an Edwards E2M30 pump. A 10-ring drift tube sealed inside a heavy wall glass tube guides the reagent ions and controls the ion-molecule reaction time. Each stainless steel ring is 7-mm thick with a 40-mm OD and a 14-mm diameter center hole. The rings are connected in series by three Teflon rods and isolated by 3.2 mm nylon spacers. Contiguous rings are connected by a  $1.0 \pm 5\%$   $\text{M}\Omega$  resistor. A negative voltage

(V2=−32 V) is typically set to develop an electric field in the drift tube. The reagent and product ions are introduced to the MS system through a pinhole of 400 μm, which is also biased by −3 V (V3). Two high vacuum stages housing the quadrupole and the electron multiplier are pumped by two Varian VT-551 turbo molecular pumps with a Varian DS402 backing pump. During measurements, the dry scroll pump draws a flow of 200 slpm ambient air into the inlet, one liter of which is drawn into the drift tube through the front orifice. A flow of N<sub>2</sub> carrying the reagent ions mixes with the air sample within the drift tube and the ion-molecule reaction proceeds throughout the drift region. The typical pressure inside the drift tube is 2.8 torr. The reagent and the product ions are analyzed by an Extrel 150-QC mass spectrometer controlled by the Merlin 3.0 software (Extrel).

The unique character of the ID-CIMS lies in that it enables quantification of neutral species by controlling the ion-molecule reaction time ( $\Delta t$ ),



where A corresponds to the neutral species to be analyzed and quantified, R represents the reagent ion, k is the reaction rate constant, and P denotes the product ion. Because Reaction 12 is kinetically limited (R>>P), the relationship between the ion signals, the ion-molecule reaction rate coefficient, the initial analyte concentration, and the reaction time  $\Delta t$  is given by:

$$[A] = \frac{[P^-]}{k\Delta t[R^-]} \quad (R13)$$

where [P<sup>−</sup>] and [R<sup>−</sup>] correspond to the intensities of product and reagent ions measured by the mass spectrometer, respectively. k can be obtained by laboratory measurements or theoretical calculations (Zhao et al., 2004a; 2004b).  $\Delta t$  is determined by the length of the drift tube and the velocity of the reagent ions, U. While moving along the drift region with the carrier gas at a flow velocity of ( $U_f$ ), ions are also driven by the controllable electric field to achieve a drift velocity ( $U_d$ ), which is determined by

$$U_d = \mu E \quad (R14)$$

where  $\mu$  is the ionic mobility and E is the electric field intensity.  $\mu$  can be calculated from the reduced ionic mobility,  $\mu_0$ ,

$$\mu = \mu_0 (760/P)(T/273.16) \quad (R15)$$

where P and T are the pressure and temperature inside the drift tube, respectively. The typical reaction time inside the drift tube is 2.6 ms.

## 2.2 Ion chemistry

The ion chemistry used to detect HNO<sub>3</sub> is similar to that described by Huey and Lovejoy (1996). The reagent ion, SiF<sub>5</sub><sup>−</sup>, is produced in two steps. A flow of about 300 standard cubic centimeters per minute (sccm) N<sub>2</sub> doped with ~0.1% SF<sub>6</sub> flows through the ion source region, where an electron attaches to the SF<sub>6</sub>.



A trace amount of SiF<sub>4</sub> is introduced downstream of the ion source and reacts with SF<sub>6</sub><sup>−</sup> through a fluoride transfer reaction to produce SiF<sub>5</sub><sup>−</sup>.



Typically, the residual SF<sub>6</sub><sup>−</sup> is less than 2% of the <sup>28</sup>SiF<sub>5</sub><sup>−</sup> reagent ions signal, which is over a million counts per second (cps). SiF<sub>5</sub><sup>−</sup> subsequently reacts with HNO<sub>3</sub> at a rate of (3.8±1)×10<sup>−10</sup> cm<sup>3</sup> molecule<sup>−1</sup> s<sup>−1</sup> (Huey and Lovejoy, 1996) to form the SiF<sub>5</sub><sup>−</sup>·HNO<sub>3</sub> adduct.



During the field campaign, the count rates of the reagent ion (corresponding to the isotope peak at *m/z* 125, <sup>30</sup>SiF<sub>5</sub><sup>−</sup>, typically 50 kilo cps) and the product ion, SiF<sub>5</sub><sup>−</sup>·HNO<sub>3</sub> (*m/z*=186) are recorded consecutively and the integration time is 50 ms and 9 s, respectively. SiF<sub>5</sub><sup>−</sup> can form weak clusters with water (Huey and Lovejoy, 1996), but we observe no water clusters in the mass spectrum. A possible explanation is that this water cluster is weakly bonded so it is readily broken up by the collisions – typically 3 Townsend (Td) – in the drift tube.

N<sub>2</sub>O<sub>5</sub> is detected using the I<sup>−</sup> reagent ion, which is generated inside the ion source through an electron attachment reaction,



N<sub>2</sub>O<sub>5</sub> subsequently reacts with I<sup>−</sup> to produce NO<sub>3</sub><sup>−</sup>, with a rate constant of 1.3×10<sup>−9</sup> cm<sup>3</sup> molecule<sup>−1</sup>s<sup>−1</sup> (Huey et al., 1995).



I<sup>−</sup> also reacts with peroxyacetyl nitrates (PAN) to form carboxylate ions (Slusher et al., 2004), but this does not interfere with N<sub>2</sub>O<sub>5</sub> measurements.

The reduced ionic mobilities ( $\mu_0$ ) of SiF<sub>5</sub><sup>−</sup> and I<sup>−</sup> have not been reported in the literature. In this work, we determine their values using theoretical calculations. A detailed description of this methodology is provided in appendix A. The values of  $\mu_0$  for SiF<sub>5</sub><sup>−</sup> and I<sup>−</sup> used are 1.89 and 2.09 cm<sup>2</sup> × V<sup>−1</sup> × s<sup>−1</sup>, respectively.

### 2.3 Instrument calibrations

The ID-CIMS can quantitatively determine the concentration of neutral species using Eq. 13. The accuracy of the calculation is affected by uncertainties associated with several parameters, including the reduced ionic mobility, the ion-molecule reaction rate constants, the transmission efficiencies of the quadrupole mass filter, fragmentation in the ion-molecule reaction, etc. These parameters are invariant under a given experimental temperature, especially when the ion-molecule reaction is collision-limited. Furthermore, their uncertainties can be determined by calibration with gas standards of a known concentration.

The  $\text{HNO}_3$  calibration employs a permeation device (component *a* in Fig. 1), which is temperature-controlled at 40°C. About a 400 to 500 sccm  $\text{N}_2$  carrier gas is fed into the side filled with glass beads and heated to the same temperature as the entire device before entering the permeation tube. After the permeation device, the concentrated  $\text{HNO}_3/\text{N}_2$  flow with a concentration of 75 to 94 ppb is injected into a 2.5 cm OD Teflon tube in which it is mixed with a 20 to 150 slpm filtered ambient air. The concentrations of the exiting  $\text{HNO}_3$  flow ranges between 0.25 and 2 ppb. Prior to each calibration, the permeation device is maintained at an operational condition for more than 6 h to achieve equilibrium.

Due to the “sticky” nature of  $\text{HNO}_3$ , it is necessary to verify the effective permeation rate under the normal operation condition to account for any possible wall loss during the preparation of the calibration standards. The procedure to verify the permeation rate is similar to the calibration process, but, instead of introducing the  $\text{HNO}_3$  standards into the ID-CIMS for calibration, the  $\text{HNO}_3$  standard is introduced to a glass bubbler containing a specific amount of pure water ( $R > 17 \text{ M}\Omega$ ) for a specific time. All tubing is passivated by the  $\text{HNO}_3$  standard for a few hours before the final solution is collected. The  $\text{HNO}_3$  solution is analyzed by ion chromatography (DIONEX), which is calibrated by ultra pure sodium nitrate (Sigma-Aldrich) solutions. The measured permeation rate is  $109 \pm 1.2 \text{ ng/min}$ , within 10% of the manufacturer’s certified value (116 ng/min).

Figure 2 shows a correlation between the volumetrically determined  $\text{HNO}_3$  standard concentration and the calculated concentration using the procedure described in Sect. 2.1. The error bars represent the systematic variation in measurements. The value of the slope in Fig. 2 corresponds to the calibration factor used to quantify the uncertainties introduced from the calculation parameters, i.e., the ion-molecule reaction rate constant, reduced ionic mobility, quadrupole transmission efficiency, etc. A calibration factor of  $2.2 \pm 0.2$  is obtained from five independent calibrations at 25°C.

$\text{N}_2\text{O}_5$  calibration is conducted with laboratory synthesized samples (Huey et al., 1995).  $\text{N}_2\text{O}_5$  is formed through two sequential Reactions 9 and 10.  $\text{O}_3$  and  $\text{NO}_2$  are mixed in a sealed glass reactor and the produced  $\text{N}_2\text{O}_5$  is collected in a cryotrap ( $-78.5^\circ\text{C}$ ) as white crystal. The first

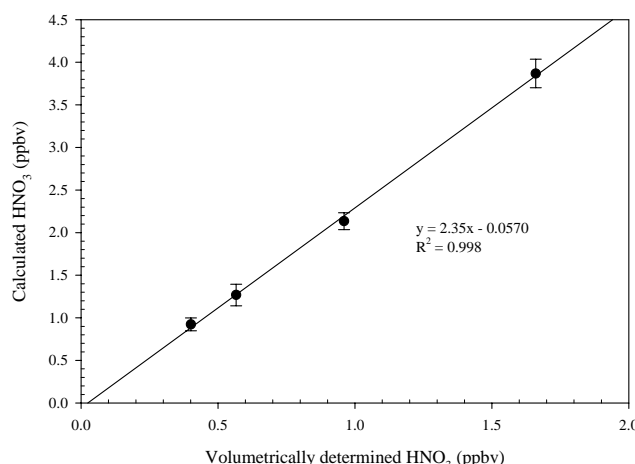


**Fig. 2.** Plot of calculated versus volumetrically prepared  $\text{HNO}_3$  concentrations. The slope corresponds to the calibration factor.

S

batch of  $\text{N}_2\text{O}_5$  is discarded to remove the water residue inside the cryotrap to minimize  $\text{HNO}_3$  formation. During calibration, pure  $\text{N}_2\text{O}_5$  is kept in an octanol/dry ice bath ( $-57^\circ\text{C}$ ). A small amount of dry  $\text{N}_2$  flows through the container and carries  $\text{N}_2\text{O}_5$  vapor into a 10-cm long absorption cell inside a UV/VIS spectrometer (Perkin Elmer), where the absolute concentration of  $\text{N}_2\text{O}_5$  is measured by its absorption at 215 nm ( $\sigma = 2.95 \times 10^{-18} \text{ cm}^2 \text{ molecule}^{-1}$ , JPL 2006). Because  $\text{HNO}_3$  has a weak absorption at 215 nm ( $\sigma = 3.66 \times 10^{-19} \text{ cm}^2 \text{ molecule}^{-1}$ , JPL 2006), the impurity of  $\text{HNO}_3$  inside the  $\text{N}_2\text{O}_5$  reservoir is further quantitated with the ID-CIMS. The results indicate the  $\text{HNO}_3$  concentration is less than 5% of the  $\text{N}_2\text{O}_5$  concentration. Thus, the  $\text{HNO}_3$  interference is small for the  $\text{N}_2\text{O}_5$  absolute calibration. The concentrated  $\text{N}_2\text{O}_5$  flow is diluted into a 140 slpm flow of  $\text{N}_2$  and analyzed by the ID-CIMS. Figure 3 shows  $\text{N}_2\text{O}_5$  concentrations measured by ID-CIMS against the concentrations determined from UV absorption. The slope in Fig. 3 represents the calibration factor.

During field measurements,  $\text{HNO}_3$  background checks are performed once every few hours by directing the ambient air flow through a 5 cm diameter nylon filter.  $\text{N}_2\text{O}_5$  background signal is checked by passing the ambient air mixed with several hundred ppb of NO through a 31 cm long heated metal tubing. The estimated detection limits of  $\text{HNO}_3$  and  $\text{N}_2\text{O}_5$  are about 38 ppt and 30 ppt for 5-min and 10-s average time, respectively, based on three times the standard deviation of the baseline signals.

### 2.4 Field setup and characterization of the inlet

The ID-CIMS instrument was deployed at the T0 super-site, located at the Instituto Mexicano del Petróleo (IMP) near the center of the Mexico City Basin ( $19^\circ 29.400' \text{ N}$ ,

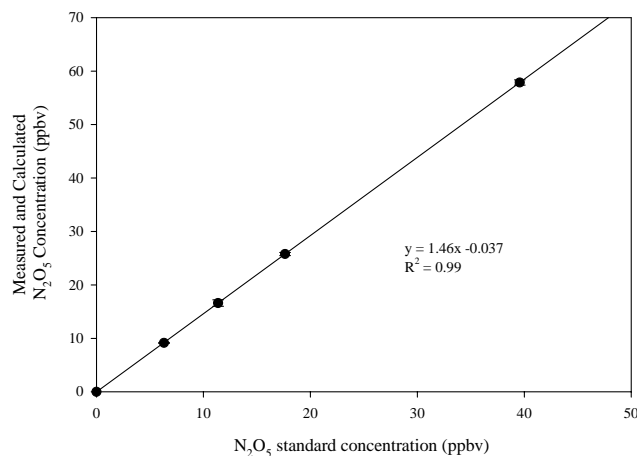


**Fig. 3.** Plot of measured and calculated N<sub>2</sub>O<sub>5</sub> vs. synthesized standards concentration. The slope corresponds to the calibration factor.

99° 08.911' W). The ID-CIMS was housed inside an air-conditioned hut on the roof top of building 32, which was about 30 m above the ground and among a cluster of buildings of similar height. A 2.20-cm ID PFA tubing was used as the inlet, which has been suggested as the best inlet material (Neuman et al., 1999). In order to minimize the surface effects, ambient air was sampled from two feet above the hut ceiling, and the inlet length was about 12 ft to bring the air sample into the ID-CIMS, located a few inches away from the sampling window. From 7 March to 29 March, the average ambient relative humidity (RH) was 41% and the maximum and the minimum temperatures were 30 and 9°C, respectively. There was no precipitation during most days of the campaign except from 24 to 29 March there were several nighttime and afternoon showers. Because HNO<sub>3</sub> gas-aerosol partitioning is sensitive to temperature, the HNO<sub>3</sub> inlet was unheated. Instead, the sampling flow rate was kept at 200 slpm to minimize the sampling residence time (0.42 s) and the entire inlet was kept under ambient conditions. We found that a smaller tubing (0.6 cm) for the inlet reduced the residence time and caused the pressure inside the drift tube to drop considerably, leading to a much shorter ion-molecule reaction time and lower sensitivity.

In order to characterize the performance of the inlet, several tests were conducted by exposing the inlet to elevated HNO<sub>3</sub> (performed at 760 torr, 25°C, and RH=50%). The front of the inlet was exposed to a solution of 68 wt% HNO<sub>3</sub> for less than one second and the ID-CIMS was set to collect data at 0.4 Hz. As shown in Fig. 4, a spike of about 40 ppb HNO<sub>3</sub> was detected by the ID-CIMS within 3 s and the HNO<sub>3</sub> signal decreased by about 80% after 9 s. The decay in the HNO<sub>3</sub> signal was fitted by an exponential decay function ([HNO<sub>3</sub>]=2.4+97.5 exp(-0.237t)). This implies that the memory effect between adjacent data points was less than 20% if data were averaged every 9 s. However, background

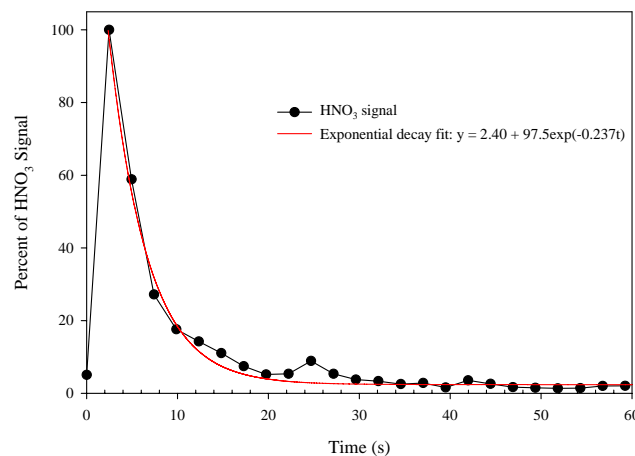


**Fig. 4.** Spike test of the inlet using a 68 wt% HNO<sub>3</sub> solution exposed to the 12 ft inlet for less than one second. The data were collected at 0.4 Hz.

checks during the field campaign showed that it usually took nearly two minutes to zero the signal when the nylon filter was installed in the front of the inlet. Therefore, we report the data in 5-min average to eliminate the memory effect.

The inlet for N<sub>2</sub>O<sub>5</sub> measurements was made from 2.2-cm ID Teflon tubing. Because we found that N<sub>2</sub>O<sub>5</sub> could be permanently lost on the inlet surface due to Reaction 11 during laboratory tests, its length was limited to 2 ft.

## 2.5 Other instrumentation at T0

An Aerodyne High-Resolution Time-of-Flight Aerosol Mass Spectrometer (HR-ToF-AMS) was used to measure the chemical composition of submicron non-refractory aerosols. This version of the AMS was capable of analyzing organic species and most nitrate and sulfate compounds of different elemental compositions at the same nominal *m/z*. More details about the AMS are given by DeCarlo et al. (2006) and Canagaratna et al. (2007). Aerosol nitrate concentrations are reported at local temperature and pressure, and should be multiplied by approx. 1.42 to obtain concentrations under standard conditions (STP, 1 atm and 273 K).

An ICMS was employed to measure both gas and aerosol phase acids at T0. A 0.6 cm ID PFA tubing with a length of about 4 m was used as an inlet. The inlet was set about 0.5 m above the roof to minimize surface effects. About 7 slpm air was pumped through the inlet to minimize the residence time. The line was directly connected to the denuder with a self constructed Teflon fitting. About 2 slpm of the air was aspirated through a wet effluent diffusion denuder (WEDD) to sample the gas phase acids. Water was continuously pumped through the denuder at a flow rate of 2 ml/min at counter flow to the air. The air to the aerosol collector (AC) was first passed through an activated charcoal denuder at 4 slpm to remove the gas phase species. The air stream was

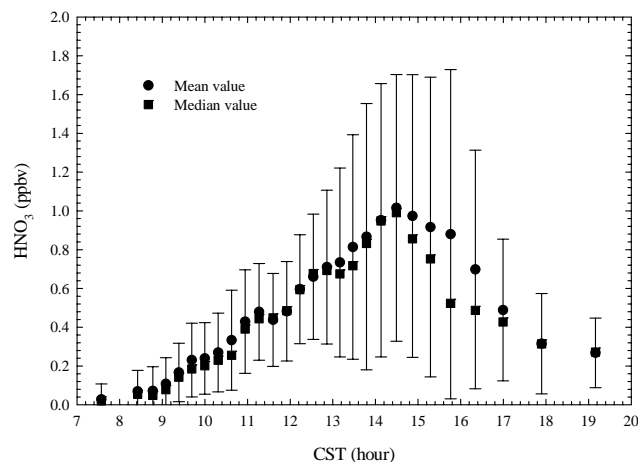


**Fig. 5.** Averaged  $\text{HNO}_3$  diurnal profile during the entire field campaign. Each point is based on 1755 data points and the error bars represent one standard deviation.

mixed with heated water vapor (at 100°C and with a flow rate of 0.6 ml/min), which condensed on aerosol particles. The droplets then impacted on a cooled maze – for details see Fisseha et al. (2006). The gas phase as well as the particle phase extracts were collected each on a concentrator column (TAC-LP1, Dionex) and analyzed alternately using ion chromatography (conductivity detector) with a mass spectrometer in a quasi-continuous mode. The mass spectrometer (MSQ from Dionex) used electro-spray ionization and had a single quadrupole mass detector. The typical detection limit for  $\text{HNO}_3$  was 0.06 ppb.

$\text{OH}$  radicals were measured at T0 using a laser-induced fluorescence instrument developed at Indiana University. A detailed description of the instrument has been provided by Dusander et al. (2008). Briefly, it is based on fluorescence assay by gas expansion technique (FAGE) and  $\text{OH}$  is directly excited and detected at 308 nm. During the MCMA-2006 campaign, the FAGE sample cell was installed on the roof top for inletless sampling. The 30-min average detection limit of FAGE during the campaign ranging from  $5 \times 10^5$  to  $2.6 \times 10^6$  molecule/cm<sup>3</sup> of  $\text{OH}$ .

$\text{NO}_x$  and  $\text{O}_3$  concentrations used in this work were measured by commercial instruments (Thermo Scientific and Teledyne 400E, respectively), which were regularly calibrated during the campaign. The 5-min average detection limits were 0.1 ppb for both species. The photolysis frequency of  $\text{O}_3$  ( $J_{\text{O}_3}$ ) was measured by spectroradiometry, and the technique was described by Volkamer et al. (2007).

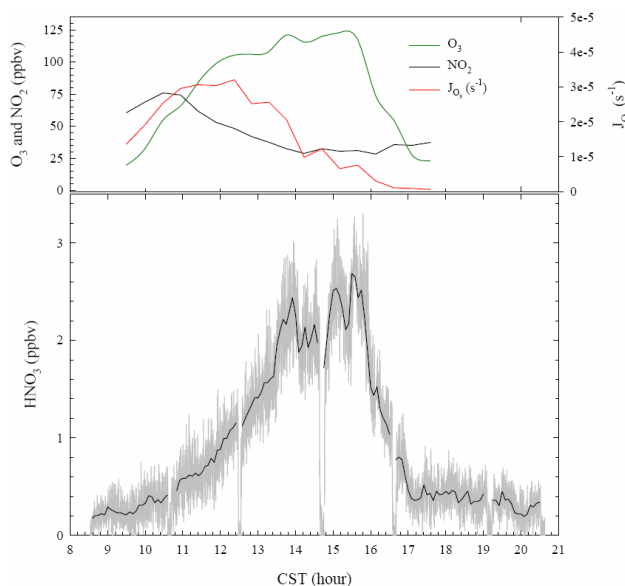


**Fig. 6.** Time series of  $\text{HNO}_3$ ,  $\text{O}_3$ ,  $\text{NO}_2$ , and  $J_{\text{O}_3}$  observed on 22 March 2006. Backgrounds of  $\text{HNO}_3$  were checked at 08:36, 10:38, 12:30, 14:39, 16:35, 19:20, and 20:35 CST. The solid lines were 5 min average data and the grey area is the 10 s raw data.

### 3 Results and discussion

#### 3.1 $\text{HNO}_3$ measurements

The measurements of  $\text{HNO}_3$  and  $\text{N}_2\text{O}_5$  were conducted from 7 to 30 March during the MCMA-2006. Due to a power supply failure, no measurements were made from 13 to 17 March. The ID-CIMS was typically configured to measure  $\text{HNO}_3$  during daytime and after sunset it was switched to the  $\text{N}_2\text{O}_5$  measurement mode. All data was collected at 0.1 Hz and presented in Central Standard Time (CST). To minimize the inlet memory effect, all  $\text{HNO}_3$  data are reported in a 5-min average and the corresponding detection limit is about 38 ppt, based on three times the standard deviation of the baseline signals.

Figure 5 shows the  $\text{HNO}_3$  diurnal profile averaged over the entire campaign. Typically, no significant  $\text{HNO}_3$  is observed before 08:00 a.m., and  $\text{HNO}_3$  starts to accumulate after 09:00 a.m. and reaches a maximum value of  $1 \pm 0.65$  ppb between 02:00 to 03:00 p.m. After 04:00 p.m.,  $\text{HNO}_3$  decreases rapidly to less than 0.4 ppb at 06:00 p.m. and gradually approaches 200 ppt, before the ID-CIMS is switched to  $\text{N}_2\text{O}_5$  measurements. The occurrence of the  $\text{HNO}_3$  daily peak is consistent with its photochemical production mechanism; however the magnitude of the  $\text{HNO}_3$  peak is lower than that expected for the large  $\text{NO}_x$  emissions in the MCMA and the strong tropical solar radiation. Another interesting observation is that several hundred ppt  $\text{HNO}_3$  is still detected several hours after sunset. Since no significant  $\text{N}_2\text{O}_5$

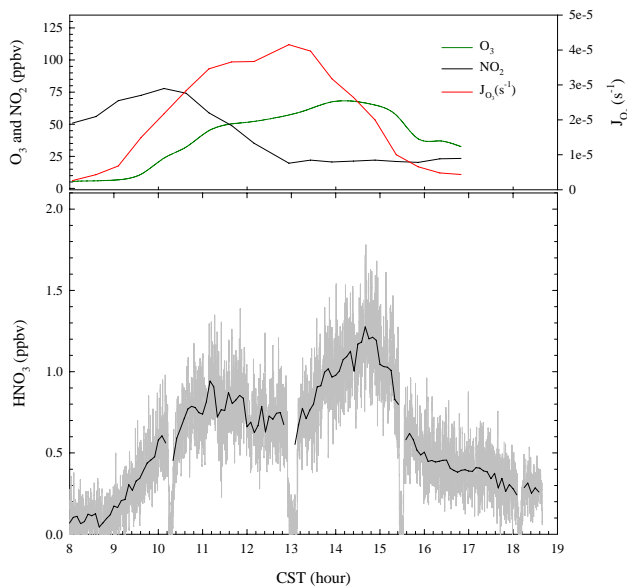


**Fig. 7.** Time series of  $\text{HNO}_3$ ,  $\text{O}_3$ ,  $\text{NO}_2$ , and  $\text{J}_{\text{O}_3}$  observed on 23 March 2006. Backgrounds were checked at 08:00, 10:15, 13:00, 15:30, and 18:10 CST. The solid lines were 5 min average data and the grey area is the 10 s raw data.

is present, the nighttime production of  $\text{HNO}_3$ , i.e. the hydrolysis of  $\text{N}_2\text{O}_5$  (through Reactions 8 to 11) does not occur.

Figure 6 shows the time series of  $\text{HNO}_3$ ,  $\text{O}_3$ ,  $\text{NO}_2$ , and  $\text{J}_{\text{O}_3}$  observed on March 22, a sunny but heavily polluted day. From 08:30 a.m. to 10:00 a.m., about 200 ppt  $\text{HNO}_3$  is observed and no significant increase occurs before 11:00 a.m., when both  $\text{NO}_2$  and  $\text{J}_{\text{O}_3}$  are near their daily maxima.  $\text{HNO}_3$  increases steadily after 11:00 a.m. and reaches a value of about 2.4 ppb at 02:00 p.m., while both  $\text{NO}_2$  and  $\text{J}_{\text{O}_3}$  are declining.  $\text{HNO}_3$  remains at its peak level from 02:00 p.m. to 04:00 p.m., and starts to decrease sharply after 04:00 p.m. due to an air mass change as is evident by a simultaneous sharp decline of ozone. Within one and half hours, only about 400 ppt is observed. The relative diurnal profile and the concentration range measured are similar to that measured in downtown Mexico City by Moya et al. (2004) using FTIR.  $\text{HNO}_3$  does not completely disappear even after it is dark, indicating that there are likely other  $\text{HNO}_3$  sources present. However, when the ID-CIMS is switched into the  $\text{N}_2\text{O}_5$  mode, no detectable  $\text{N}_2\text{O}_5$  is present (<30 ppt). One possible explanation is that the residue  $\text{HNO}_3$  is in equilibrium with the ammonium nitrate aerosol, which is also still detectable after sunset.

Figure 7 depicts time series of  $\text{HNO}_3$ ,  $\text{O}_3$ ,  $\text{NO}_2$ , and  $\text{J}_{\text{O}_3}$  observed on 23 March, a relatively cleaner day than the previous day, as inferred from the higher  $\text{J}_{\text{O}_3}$  value and lower  $\text{O}_3$  concentration on 23 March. Before 09:00 a.m.,  $\text{HNO}_3$  is close to the instrument detection limit. Shortly after 09:00 a.m.  $\text{HNO}_3$  increases steadily to about 0.9 ppb

at 11:30 a.m. and then starts to decrease to 600 ppt at 01:00 p.m., when  $\text{OH}$  production is expected to be high. Shortly after 01:00 p.m.  $\text{HNO}_3$  starts to increase again and reaches a daily maximum of 1.25 ppb. Afterwards,  $\text{HNO}_3$  decreases steadily to 400 ppt at 04:00 p.m. Similar to the previous day, a value of near 300 ppt  $\text{HNO}_3$  is still observable at about 06:30 p.m. When the ID-CIMS is switched into the  $\text{N}_2\text{O}_5$  mode, no detectable  $\text{N}_2\text{O}_5$  is present. Note that 22 and 23 March represent the typical “more polluted” and “cleaner” conditions encountered during the field campaign, respectively.

$\text{O}_3$  in Figs. 6 and 7 exhibits a similar profile as  $\text{HNO}_3$  but with a delay in the peak time compared with  $\text{J}_{\text{O}_3}$ . This is expected as both compounds are produced from two competitive reactions in the photooxidation process according to Reactions 1, 21 and 22.



As discussed above, although  $\text{HNO}_3$  production began immediately after sunrise (~06:30 a.m.), no significant accumulation of  $\text{HNO}_3$  is typically observed before 09:00 a.m. Thus, it is evident that the gas-phase chemistry alone cannot explain the observations in the  $\text{HNO}_3$  diurnal profiles, i.e., the slow rise after sunrise and the residual  $\text{HNO}_3$  after sunset. Heterogeneous processing of  $\text{HNO}_3$  in the particle-phase needs to be accounted for to explain the  $\text{HNO}_3$  measurements during MCMA 2006. The heterogeneous reaction between  $\text{HNO}_3$  and  $\text{NH}_3$  in the particle-phase to form ammonium nitrate represents an important process to modulate the gaseous  $\text{HNO}_3$  concentration,



Depending on the RH, ammonium nitrate formed in Reaction 23 exists as a solid or an aqueous solution of  $\text{NH}_4^+$  and  $\text{NO}_3^-$ . The equilibrium constant,  $K_p$ , depends on the temperature (Seinfeld and Pandis, 1998),

$$\ln K_p = 84.6 - (24220/T) - 6.1 \times \ln(T/298) \quad (\text{R24})$$

For the measurements relevant to MCMA 2006, the RH is fairly low (<41% averaged over the campaign period). The dry environment at the MCMA prevents  $\text{NH}_4\text{NO}_3$  from deliquescence and  $\text{NH}_4\text{NO}_3$  is expected to be a solid. High ammonia ( $\text{NH}_3$ ) concentrations (>35 ppb in the early morning) were reported during the MCMA 2003 campaign (Moya et al., 2004). Although no direct measurements of  $\text{NH}_3$  are available at T0 during MCMA 2006,  $\text{NH}_3$  measured at the T1 site (~30 km to the northeast of T0) using a quantum-cascade laser (QCL) spectrometer (Fischer and Littlejohn, 2007) shows an average concentration of  $26.7 \pm 13.7$  ppb from 21 to 31 March.

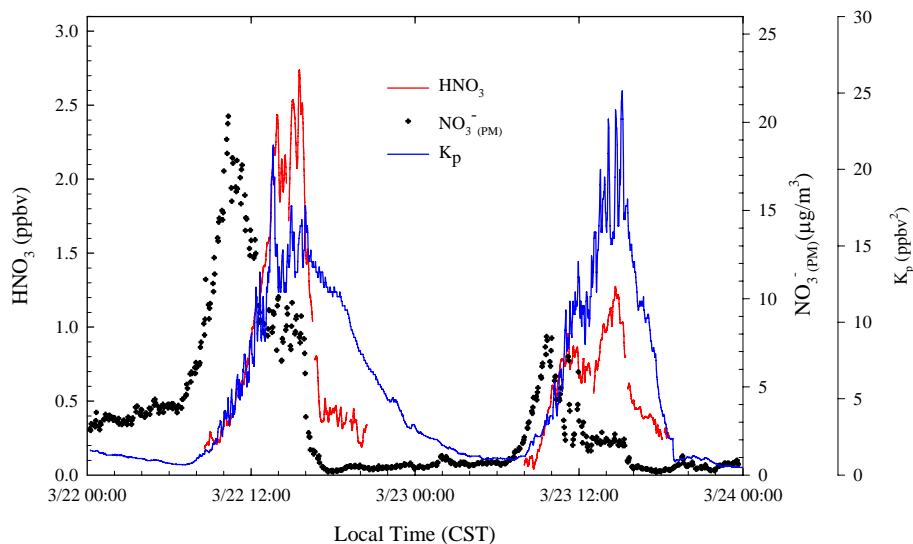


**Fig. 8.** Gaseous  $\text{HNO}_3$ , submicron aerosol nitrate ( $\text{NO}_{3(\text{PM})}^-$ ) ( $1 \mu\text{g}/\text{m}^3$  nitrate under ambient pressure and temperature can contribute to 0.51 ppb gaseous  $\text{HNO}_3$  after complete evaporation), and the calculated dissociation constant  $K_p$  of Reaction 26 for 22 and 23 March 2006.

Figure 8 shows a comparison between gaseous  $\text{HNO}_3$  and submicron aerosol nitrate ( $\text{NO}_{3(\text{PM})}^-$ ) mass concentration measured by the AMS on 22 and 23 March. The calculated equilibrium constant ( $K_p$ ) of Reaction 23 is also plotted in Fig. 8, which is a function of ambient temperature. There are several prominent features in Fig. 8. The aerosol nitrate starts to increase right after sunrise and reaches a maximum in the early morning. The aerosol nitrate peak occurs several hours earlier than that of the gaseous  $\text{HNO}_3$  concentration. The aerosol nitrate drops sharply after the morning peak and remains low throughout the afternoon and night hours. The measured  $\text{HNO}_3$  concentration and the calculated  $K_p$  are anti-correlated with  $\text{NO}_{3(\text{PM})}^-$ . On the other hand, there appears to exist a good correlation between the measured  $\text{HNO}_3$  concentration and calculated  $K_p$ : both slowly increase at the morning hours and their peaks coincide. Hence, the slow rise in the measured  $\text{HNO}_3$  concentration is likely explained by gas/aerosol partitioning.  $\text{HNO}_3$  photochemically produced from Reaction 1 is scavenged from the gas phase by the particle-phase reaction with  $\text{NH}_3$  to form aerosol nitrate, when ambient temperature is low but ammonia is high (Moya et al., 2004) and aerosol nitrate is favorable ( $K_p < 6$ ). The gas/aerosol partitioning hence likely accounts for the delayed rise and daily maximum of measured  $\text{HNO}_3$  compared to those of measured aerosol nitrate. As the temperature rises and the  $\text{NH}_3$  concentration likely decreases strongly (Moya et al., 2004) during the course of the day, the equilibrium favors gaseous  $\text{HNO}_3$ .  $\text{HNO}_3$  is released back to the gas-phase from the evaporation of aerosol nitrate, leading to a peak in the gas-phase concentration even when its photochemical production decreases. After sunset, the  $\text{HNO}_3$  photochemical production ceases, as reflected in the decrease of measured  $\text{HNO}_3$ , but a few hundreds of ppt  $\text{HNO}_3$  are still

measured. Evidently, a small increase of submicron aerosol nitrate is observed from 06:00 p.m. to about 07:30 p.m. on 22 and 23 March, while  $\text{HNO}_3$  is decreasing. At the same time, the ambient temperature is also decreasing, in favor of the conversion of gaseous  $\text{HNO}_3$  into aerosol nitrate. Therefore, the lingering nighttime  $\text{HNO}_3$  likely originates from the residue ammonium nitrate aerosol, instead of the hydrolysis of  $\text{N}_2\text{O}_5$ .

It should be pointed out that the above discussions are based on surface measurements only. However, higher concentrations of  $\text{NO}_3$  and  $\text{N}_2\text{O}_5$  above the nocturnal surface layer (and thus away from direct NO emissions) have been reported in other field studies (Brown et al., 2007; Geyer and Stutz, 2004; Stutz et al., 2004). Thus, some of the nighttime  $\text{HNO}_3$  can also be formed aloft and then transported down to the surface. Figure 8 also shows that on a daily basis a higher aerosol nitrate corresponds to a higher  $\text{HNO}_3$  peak, when the difference in  $K_p$  is insignificant. This probably explains the difference in the measurements of  $\text{NO}_{3(\text{PM})}^-$  and  $\text{HNO}_3$  between 22 and 23 March 2006. Figure 9 shows additional daily profiles of  $\text{NO}_{3(\text{PM})}^-$  and  $\text{HNO}_3$  observed on 11 and 12 March, showing a similar correlation between  $\text{NO}_{3(\text{PM})}^-$  and  $\text{HNO}_3$ . As discussed before,  $\text{HNO}_3$  is present primarily in the aerosol phase during the early morning hours due to lower temperatures and higher  $\text{NH}_3$ .  $\text{HNO}_3$  is released from  $\text{NO}_{3(\text{PM})}^-$  as the ambient air temperature rises and reaches the daily maximum around 02:00 p.m. After sunset both  $\text{NO}_{3(\text{PM})}^-$  and  $\text{HNO}_3$  decrease, but remain in detectable amounts. Therefore, we conclude that during MCMA 2006 at T0 the gas/particle partitioning plays a key role in regulating gaseous  $\text{HNO}_3$  and is essential to account for the measurements of gaseous  $\text{HNO}_3$  and aerosol nitrate.

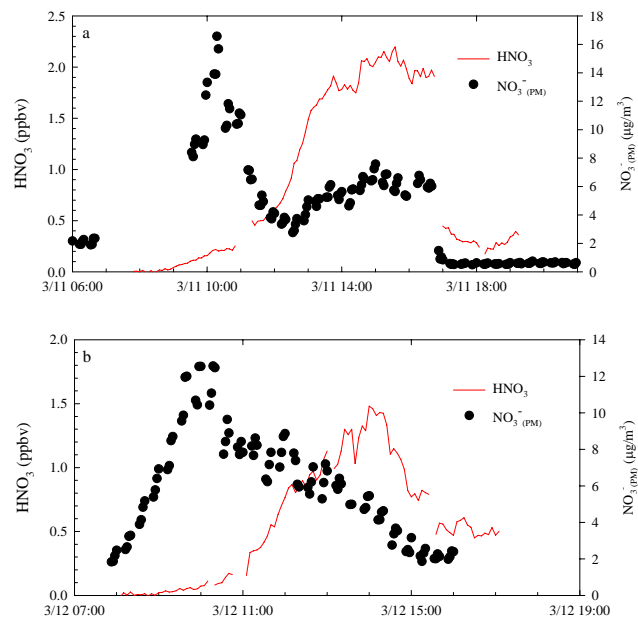


**Fig. 9.** Gaseous  $\text{HNO}_3$ , submicron aerosol nitrate ( $\text{NO}_3^-(\text{PM})$ ) observed on 11 (a) and 12 March (b).

Our results are consistent with earlier studies conducted in MCMA. Salcedo et al. (2006) measured aerosol nitrate during the MCMA 2003 campaign. They found that the morning particulate nitrate increased in a manner consistent with the production of nitric acid, but after 11:00 a.m. the aerosol nitrate decreased while  $\text{HNO}_3$  production continued. This observation was explained by the increase of the planetary boundary layer (PBL) height and temperature and the decrease in the RH and  $\text{NH}_3$  as the day progressed. Also, it has been suggested that gas-particle partitioning plays a dominant role in the fate of aerosol ammonium nitrate over larger spatial scales (DeCarlo et al., 2008).

In order to assess the  $\text{HNO}_3$  budget at T0 during MCMA 2006, we calculate the  $\text{HNO}_3$  production rate ( $P_{\text{HNO}_3}$ ) from Reaction 1 between 10:00 a.m. and 06:00 p.m. on 20 March with a rate constant recommended by Okumura and Sander (2005). The results, along with OH,  $\text{NO}_2$ ,  $\text{HNO}_3$ ,  $\text{NO}_3^-(\text{PM})$ , PBL height, and temperature measurements, are shown in Fig. 10. From 10:15 a.m. to 11:45 a.m.,  $P_{\text{HNO}_3}$  increases from near 1 ppb/hr to about 6.4 ppb/hr, while total  $\text{HNO}_3$  ( $\text{HNO}_3 + \text{submicron } \text{NO}_3^-(\text{PM})$ ) only increases moderately. This can be partially explained by the significant increase in PBL, by a factor of about 2.5. After 11:45 a.m.,  $P_{\text{HNO}_3}$  decreases to about 1.7 ppb/hr at about 12:45 p.m., which is mainly caused by the decreases of both OH and  $\text{NO}_2$ , and fluctuates near 1.7 ppb/hr thereafter. Total  $\text{HNO}_3$  peaks around early afternoon and starts decreasing after 02:30 p.m.. From the  $\text{HNO}_3$  data, we estimate a maximum total  $\text{HNO}_3$  of about 3 ppb, which is significantly less than expected from the calculated  $P_{\text{HNO}_3}$ . Thus processes such as dry deposition and reactions on dust must play a role to

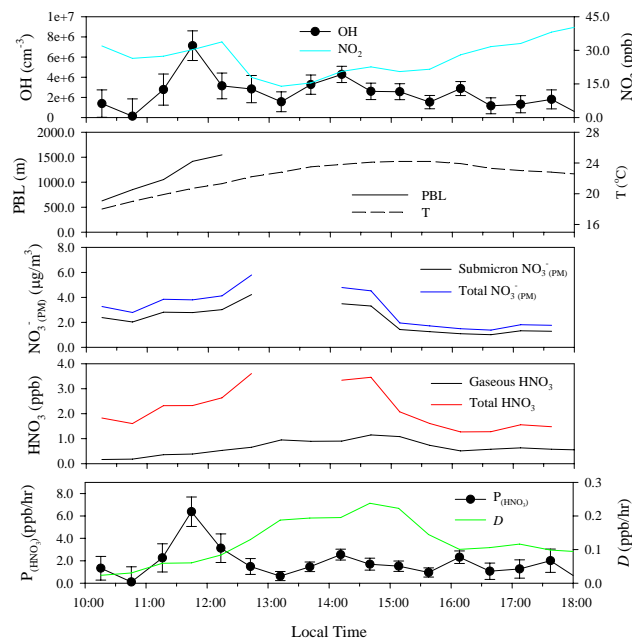


**Fig. 10.** 30 min average OH,  $\text{NO}_2$ , temperature, PBL, aerosol nitrate ( $\text{NO}_3^-(\text{PM})$ ), gaseous  $\text{HNO}_3$  and total  $\text{HNO}_3$  (assuming all  $\text{NO}_3^-(\text{PM})$  is in gas-phase), calculated  $\text{HNO}_3$  production rate ( $P_{\text{HNO}_3}$ ), and gaseous  $\text{HNO}_3$  dry deposition rate on 20 March at T0.

remove  $\text{HNO}_3$  from the ambient air in the MCMA. Heterogeneous reaction of  $\text{HNO}_3$  on dust surfaces has been shown to be important during MILAGRO, leading to permanent removal of  $\text{HNO}_3$  to form non-volatile mineral nitrates such as  $\text{Ca}(\text{NO}_3)_2$  (Querol et al., 2008; Fountoukis et al., 2007; Hodzic et al., 2007). This nitrate can exist in the supermicron size range and thus is not measured by the AMS. Querol et al. (2008) estimated nitrate content in the  $\text{PM}_{10}-\text{PM}_{2.5}$  range accounts for  $\sim 20\%$  of the total nitrate at T0, with a higher fraction in the early part of MILAGRO due to reduced precipitation and increased dust concentration. Since the AMS measures  $\text{PM}_1$  aerosols, there will be some additional nitrate associated with dust in the  $\text{PM}_{2.5}-\text{PM}_1$  range beyond that quantified by Querol et al. If the dust size distribution in Mexico is similar to that reported by Maring et al. (2003) and the dust reactivity is uniform across the dust size distribution, this size range will likely account for about  $\sim 1/3$  additional dust nitrate beyond that  $\text{PM}_{10}-\text{PM}_{2.5}$  size range, i.e.  $\sim 7\%$  of the total aerosol nitrate, such that the total nitrate can be estimated as 1.37 times the submicron nitrate. From 10:15 a.m. to 12:45 a.m., the observed increase of total  $\text{HNO}_3$  is about 1.8 ppb and 1.3 ppb of which is due to aerosol nitrate, while the total  $\text{HNO}_3$  produced from Reaction 1 is about 2.6 ppb after applying the dilution factor of 2.5. Therefore, aerosol phase nitrate and gaseous  $\text{HNO}_3$  can account for about 50% and 19% of the  $\text{HNO}_3$  produced from Reaction 1, respectively.

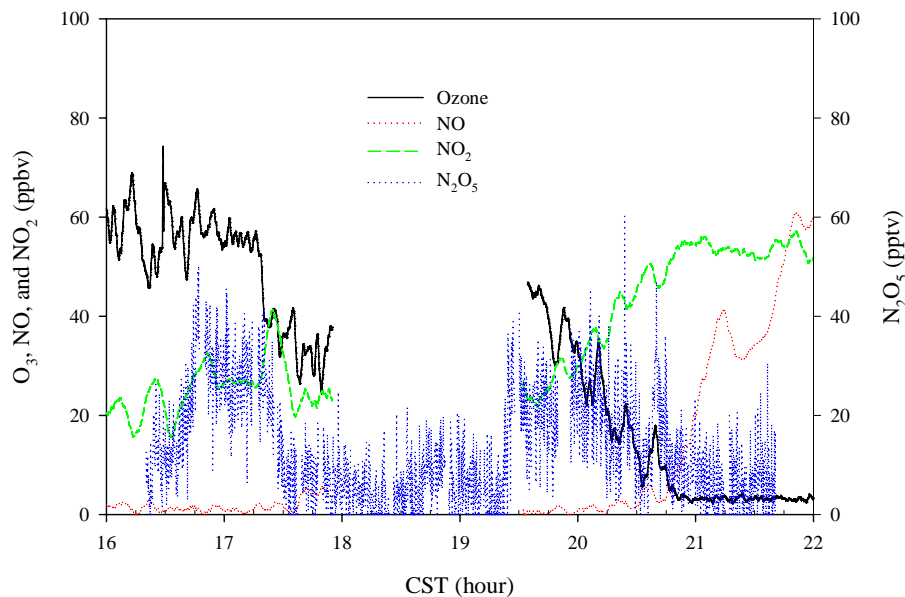


**Fig. 11.**  $\text{N}_2\text{O}_5$  measured on 26 March. Also shown are plots of NO,  $\text{NO}_2$ , and  $\text{O}_3$ . The gap in the measurements was due to instrument calibrations.

Finally we evaluate the potential effect of dry deposition on the measured  $\text{HNO}_3$  concentrations. The dry deposition ( $D$ ) can be estimated as:

$$D = v_d * C \quad (\text{R25})$$

where  $v_d$  is the deposition velocity and  $C$  is the concentration.  $v_d$  is much larger for  $\text{HNO}_3$  than aerosol nitrate (e.g. Kajino et al., 2008), and to first approximation we estimate the deposition flux by only estimating that of nitric acid.  $\text{HNO}_3$  deposition velocity is calculated according to the method described by Fast et al. (2006) and an average value of about  $5 \text{ cm s}^{-1}$  is obtained from 10:15 to 12:45 a.m., which is consistent with the literature values (Myles et al., 2007; Pryor and Klemm, 2004). Based on the observed PBL height and gaseous  $\text{HNO}_3$ , the estimated dry deposition rate (also shown in Fig. 10) would reduce  $\text{HNO}_3$  concentrations over the depth of the boundary layer by  $\sim 0.08 \text{ ppb hr}^{-1}$ , which accounts for additional 8% of the total  $\text{HNO}_3$  production. Although there is still 23% of the  $\text{HNO}_3$  production cannot be accounted for, it is well within the experimental uncertainties of all the parameters used in the estimation. Figure 10 also shows that temperature affects the partitioning between  $\text{NO}_{3(\text{PM})}^-$  and  $\text{HNO}_3$ . Temperature increases gradually from  $18^\circ\text{C}$  to  $24^\circ\text{C}$  from 10:00 a.m. to 03:00 p.m. and decreases slightly thereafter.  $\text{HNO}_3$  clearly follows a similar trend as temperature; however,  $\text{NO}_{3(\text{PM})}^-$  shows an opposite trend with higher concentrations in the morning than in the afternoon.

### 3.2 $\text{N}_2\text{O}_5$ Measurements

The ID-CIMS instrument is typically switched to measure  $\text{N}_2\text{O}_5$  after sunset during the MCMA-2006 campaign. Nighttime  $\text{N}_2\text{O}_5$  is typically below the detection limit of the instrument. Because NO concentration frequently exceeds 100 ppb after 07:00 p.m. and  $\text{O}_3$  is rapidly depleted by freshly emitted NO, Reactions 9 and 10 are inhibited at the surface level. Therefore,  $\text{NO}_3$  and  $\text{N}_2\text{O}_5$  do not play a major role during the nighttime chemistry at the surface, although it is likely that some  $\text{HNO}_3$  may be formed above the PBL where the  $\text{N}_2\text{O}_5$  chemistry is still occurring at night and mixes downward (Stutz et al., 2004). However, as an exception, two  $\text{N}_2\text{O}_5$  peaks are observed in the late afternoon and early evening on 26 March (Fig. 11). There was a scattered shower starting in the early afternoon and no  $\text{HNO}_3$  was observed thereafter. At 04:00 p.m., the rain stopped and the sky remained cloudy. The concentrations of  $\text{O}_3$  and  $\text{NO}_2$  are about 60 ppb and 20 ppb, respectively, while the NO concentration is less than 2 ppb. The ID-CIMS was switched to the  $\text{N}_2\text{O}_5$  mode at 04:20 p.m. and the measurement continued until 09:40 p.m., when NO and  $\text{NO}_2$  were about 40 ppb and 60 ppb but  $\text{O}_3$  was only 3 ppb. Background checks were performed at the beginning and at the end of the measurement. Two  $\text{N}_2\text{O}_5$  peaks near 40 ppt are observed around 05:00 p.m. and 08:00 p.m., when both  $\text{NO}_2$  and  $\text{O}_3$  are still substantial, but no fresh NO emission is present. From 05:45 p.m. to 07:20 p.m., the T0 site was hit by another intermittent shower; no  $\text{N}_2\text{O}_5$  was observed and the  $\text{NO}_x$  and  $\text{O}_3$  instruments were off-line for calibrations. After 07:30 p.m.,  $\text{O}_3$  is negatively correlated with  $\text{NO}_2$  due to Reaction 8. About 08:50 p.m., NO starts to

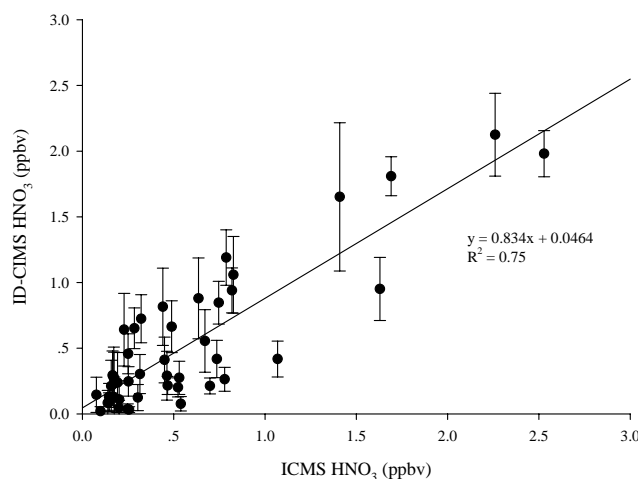
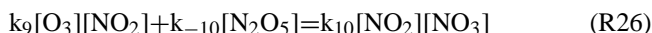


**Fig. 12.** Inter-comparison between the ID-CIMS and ICMS based on 45 overlapping data points collected from 8 to 29 March 2006.

increase significantly and nearly all O<sub>3</sub> is depleted, as N<sub>2</sub>O<sub>5</sub> disappears. The temperature during the observation period is relatively low (average 14.6°C). Since the ID-CIMS responds to both NO<sub>3</sub> and N<sub>2</sub>O<sub>5</sub> by detecting the same nitrate anion at *m/z* 62, we estimate a steady state NO<sub>3</sub> concentration based on Reactions 9 and 10, assuming that the ID-CIMS responds to NO<sub>3</sub> and N<sub>2</sub>O<sub>5</sub> equivalently:



where [NO<sub>3</sub><sup>-</sup>], k<sub>9</sub>, k<sub>10</sub>, and k<sub>-10</sub> are the total NO<sub>3</sub><sup>-</sup> signal observed by the ID-CIMS, the rate constant of Reaction 9, the forward reaction rate constant of Reaction 10, and the reverse reaction rate constant of Reaction 10, respectively. k<sub>9</sub>, k<sub>10</sub>, and k<sub>-10</sub> are calculated according to formulas recommended by JPL (2006). The results suggest that NO<sub>3</sub> radical account for less than 4% of the total signal.

### 3.3 Inter-comparison with ICMS

An ICMS instrument is set up side-by-side with the ID-CIMS during the MCMA-2006 field campaign. The ICMS utilizes a denuder to selectively collect gas phase HNO<sub>3</sub> into aqueous solutions, which are then analyzed by an electrospray mass spectrometer. Since the ICMS produce one data point about every two hours, its time series does not match with the temporal resolution of about 10 s from the ID-CIMS measurements. We compare the results between the two instruments for periods when both instruments are collecting data and the ID-CIMS data are averaged to represent the data during a similar period. The results are plotted in Fig. 12, showing a good correlation (*R*<sup>2</sup>=0.75) between the two techniques. We also perform a *t*-test for these two sets of data and a significance value of 0.68 further confirms that statistically the re-

sults from the two techniques are in good agreement. The ID-CIMS data are about 17% lower than the ICMS data, and the y-intercept is much smaller than the detection limit of either instrument. However, because the overlapping data points are rather scarce, the positive trend at low values is not as good as at the higher values. One possible explanation is that the variations of HNO<sub>3</sub> (indicated by the error bars) affect the correlation more significantly at low concentrations than at high concentrations. Also, the error bars can account for the difference in response time between the two instruments, i.e. a higher level of variation indicates faster changing of HNO<sub>3</sub>, which is easily captured by the ID-CIMS.

## 4 Conclusions

An ID-CIMS instrument was deployed during the MCMA-2006 campaign to measure HNO<sub>3</sub> and N<sub>2</sub>O<sub>5</sub> at the T0 urban site. The objective of this work is to characterize the NO<sub>x</sub> chemistry and budget in the MCMA. Diurnally, HNO<sub>3</sub> is less than 200 ppt during the night and in the early morning, increases steadily from around 09:00 a.m. CST, reaches a peak value of 0.5 to 3 ppb in the early afternoon, and then declines sharply to less than half of the peak value near 05:00 p.m. CST. The HNO<sub>3</sub> mixing ratio is found to negatively correlate with submicron aerosol nitrate, suggesting that the gaseous HNO<sub>3</sub> concentration is primarily produced by the photochemistry and regulated by the gas-particle partitioning process. Gaseous HNO<sub>3</sub> and submicron aerosol nitrate can account for 19% and 36% of the calculated HNO<sub>3</sub> production rate based on OH and NO<sub>2</sub> observations. Dry deposition can only explain about 8% of the total HNO<sub>3</sub> production. However, additional losses by HNO<sub>3</sub> reaction on dust particles likely contribute to about another 14% of the total HNO<sub>3</sub> production. Thus, only 23% of the HNO<sub>3</sub> production cannot be accounted for but it is well within the experimental uncertainties. Inter-comparison between the ID-CIMS and the ICMS shows a good agreement (*R*<sup>2</sup>=0.75) in the HNO<sub>3</sub> measurements. During most times of the MCMA-2006 campaign, N<sub>2</sub>O<sub>5</sub> is below the detection limit of the ID-CIMS due to high NO mixing ratio at the surface, except on one occasion on 26 March when transient N<sub>2</sub>O<sub>5</sub> peaks of 40 ppt are detected under cloudy conditions. At the surface, N<sub>2</sub>O<sub>5</sub> appears to play a minor role in HNO<sub>3</sub> production, but it still can exist in significant concentration in the upper boundary layer and undergoes heterogeneous reactions to form HNO<sub>3</sub>, which can be transported to the surface.

## Appendix A

The reduced ionic mobilities,  $\mu_0$ , of  $\text{SiF}_5^-$  and  $\text{I}^-$  are not reported in the literature. In this work, we determine their values according to Mason and McDaniel (1988),

$$\mu_0 = \frac{1.85 \times 10^4}{\bar{\Omega} \sqrt{T_{\text{eff}}}} \left( \frac{m+M}{mM} \right)^{1/2} \text{cm}^2 \times V^{-1} \times s^{-1}, \quad (\text{A1})$$

where  $T_{\text{eff}}$  is the effective temperature of the carrier gas (in K),  $m$  and  $M$  are the masses (in atomic mass units) of the ion ( $\text{SiF}_5^-$  or  $\text{I}^-$ ) and the carrier gas ( $\text{N}_2$ ), respectively, and  $\bar{\Omega}$  is the momentum-transfer collision integral (in  $\text{cm}^2$ ).  $T_{\text{eff}}$  is given by

$$\frac{3}{2} k_b T_{\text{eff}} = \frac{3}{2} k_b T + \frac{1}{2} m U_f^2 \quad (\text{A2})$$

where  $k_b$  is Boltzmann's constant and  $T$  is the temperature of the carrier gas.  $\bar{\Omega}$  is obtained from the tabulated values (Viehland et al., 1975) based on ion-neutral interaction potentials. Because no experimental data are available to characterize the ion-neutral interactions in the  $\text{SiF}_5^-/\text{N}_2$  or  $\text{I}^-/\text{N}_2$  system, we perform ab initio calculations to obtain the ion-neutral interaction potentials using the Gaussian 03 software package on an SGI Origin 3800 supercomputer (Lei et al., 2000; Suh et al., 2002; Zhang et al., 2002; Suh et al., 2003). The geometry optimization and energy calculations at a series of center-to-center distances for  $\text{SiF}_5^-/\text{N}_2$  and  $\text{I}^-/\text{N}_2$  systems are conducted using density function method B3LYP/6-31G(d,p) and B3LYP/LANL2DZ, respectively. The results are then fitted with a potential model (Viehland et al., 1975)

$$V(r) = \frac{B}{r^{12}} - \frac{C_6}{r^6} - \frac{C_4}{r^4} \quad (\text{A3})$$

where the  $B$  term represents the short-range repulsion energy,  $C_6$  denotes the charge-induced quadrupole attraction plus the London dispersion attraction, and  $C_4$  represents the attraction between the ion and the dipole induced in  $\text{N}_2$ . Based on the calculated potential well depth,  $\varepsilon$ , and the minimum position,  $r_m$ , the corresponding value of  $\bar{\Omega}$  is obtained. Table A1 provides a summary of the calculations. The predicted values of  $\mu_0$  for  $\text{SiF}_5^-$  and  $\text{I}^-$  are 1.89 and  $2.09 \text{ cm}^2 \times V^{-1} \times s^{-1}$ , respectively.

**Acknowledgements.** This research was funded by the Center for Atmospheric Chemistry and Environment at the Texas A&M University and by the Robert A. Welch Foundation (Grant A-1417). Additional support was provided by the Texas A&M University Supercomputing Facilities. The authors are grateful to Nancy A. Marley and Jeffrey S. Gaffney for providing the temperature and RH data, Jerome D. Fast for providing calculated  $\text{HNO}_3$  dry deposition rates, William E. Eichinger for providing boundary height data at T0, and Marc L. Fischer for providing  $\text{NH}_3$  data at T1 site. A. C. A. and J. L. J. acknowledged support from NSF (ATM-0449815 and ATM-0528634), DOE (BER, ASP program, DE-FG02-05ER63981), and a NASA Graduate Fellowship to ACA

**Table A1.** Ion-neutral potentials of  $\text{SiF}_5^-/\text{N}_2$  and  $\text{I}^-/\text{N}_2$  systems based on *ab initio* calculations

	$\text{SiF}_5^-/\text{N}_2$	$\text{I}^-/\text{N}_2$
$\varepsilon$ (eV)	0.050	0.057
$r_m$ (Å)	4.82	4.06
$B$ (eV·Å <sup>12</sup> )	$8.62 \times 10^6$	$5.29 \times 10^5$
$C_6$ (eV·Å <sup>6</sup> )	824.96	220.38
$C_4$ (eV·Å <sup>4</sup> )	20.98	8.39
$\bar{\Omega}$ (10 <sup>-16</sup> cm <sup>2</sup> )	73.16	51.83

(NNG04GR06H), K. G. and J. D. acknowledged support from SNSF and INTROP (1024, 1034), and L. T. M. acknowledged support from NSF (ATM-0528227).

Edited by: S. Madronich

## References

- Anlauf, K. G., Mactavish, D. C., Wiebe, H. A., Schiff, H. I., and Mackay, G. I.: Measurement of atmospheric nitric-acid by the filter method and comparisons with the tunable diode-laser and other methods, *Atmos. Environ.*, 22, 1579–1586, 1988.
- Brown, S. S., Stark, H., Ciciora, S. J., and Ravishankara, A. R.: In-situ measurement of atmospheric  $\text{NO}_3$  and  $\text{N}_2\text{O}_5$  via cavity ring-down spectroscopy, *Geophys. Res. Lett.*, 28, 3227–3230, 2001.
- Brown, S. S., Stark, H., Ciciora, S. J., McLaughlin, R. J., and Ravishankara, A. R.: Simultaneous in situ detection of atmospheric  $\text{NO}_3$  and  $\text{N}_2\text{O}_5$  via cavity ring-down spectroscopy, *Rev. Sci. Instrum.*, 73, 3291–3301, 2002.
- Brown, S. S., Ryerson, T. B., Wollny, A. G., Brock, C. A., Peltier, R., Sullivan, A. P., Weber, R. J., Dube, W. P., Trainer, M., Meagher, J. F., Fehsenfeld, F. C., and Ravishankara, A. R.: Variability in nocturnal nitrogen oxide processing and its role in regional air quality, *Science*, 311, 67–70, 2006.
- Brown, S. S., Dube, W. P., Osthoff, H. D., Stutz, J., Ryerson, T. B., Wollny, A. G., Brock, C. A., Warneke, C., De Gouw, J. A., Atlas, E., Neuman, J. A., Holloway, J. S., Lerner, B. M., Williams, E. J., Kuster, W. C., Goldan, P. D., Angevine, W. M., Trainer, M., Fehsenfeld, F. C., and Ravishankara, A. R.: Vertical profiles in  $\text{NO}_3$  and  $\text{N}_2\text{O}_5$  measured from an aircraft: Results from the NOAA P-3 and surface platforms during the new England air quality study 2004, *J. Geophys. Res.-Atmos.*, 112, D22304, doi:10.1029/2007JD008883, 2007.
- CAM (Comisión Ambiental Metropolitana): *Inventario de emisiones 2004 de la Zona Metropolitana del Valle de México*, Secretaría del Medio Ambiente, Gobierno de México, México, online available at: <http://www.sma.df.gob.mx/>, 2006.
- Canagaratna, M. R., Jayne, J. T., Jimenez, J. L., Allan, J. D., Alfarra, M. R., Zhang, Q., Onasch, T. B., Drewnick, F., Coe, H., Middlebrook, A., Delia, A., Williams, L. R., Trimborn, A. M., Northway, M. J., DeCarlo, P. F., Kolb, C. E., Davidovits, P., and Worsnop, D. R.: Chemical and Microphysical Characterization of Ambient Aerosols with the Aerodyne Aerosol Mass Spectrometer, *Mass Spectrom. Rev.*, 26, 185–222, 2007.

- DeCarlo, P. F., Kimmel, J. R., Trimborn, A., Northway, M. J., Jayne, J. T., Aiken, A. C., Gonin, M., Fuhrer, K., Horvath, T., Docherty, K. S., Worsnop, D. R., and Jimenez, J. L.: Field-deployable, high-resolution, time-of-flight aerosol mass spectrometer, *Anal. Chem.*, 78, 8281–8289, 2006.
- DeCarlo, P. F., Dunlea, E. J., Kimmel, J. R., Aiken, A. C., Sueper, D., Crounse, J., Wennberg, P. O., Emmons, L., Shinozuka, Y., Clarke, A., Zhou, J., Tomlinson, J., Collins, D. R., Knapp, D., Weinheimer, A. J., Montzka, D. D., Campos, T., and Jimenez, J. L.: Fast airborne aerosol size and chemistry measurements above Mexico City and Central Mexico during the MILAGRO campaign, *Atmos. Chem. Phys.*, 8, 4027–4048, 2008, <http://www.atmos-chem-phys.net/8/4027/2008/>.
- Dusanter, S., Vimal, D., Stevens, P. S., Volkamer, R., and Molina, L. T.: Measurements of OH and HO<sub>2</sub> concentrations during the MCMA-2006 field campaign – Part 1: Deployment of the Indiana University laser-induced fluorescence instrument, *Atmos. Chem. Phys. Discuss.*, 8, 13 689–13 739, 2008, <http://www.atmos-chem-phys-discuss.net/8/13689/2008/>.
- Fast, J. D., Gustafson, W. I., Easter, R. C., Zaveri, R. A., Barnard, J. C., Chapman, E. G., Grell, G. A., and Peckham, S. E.: Evolution of ozone, particulates, and aerosol direct radiative forcing in the vicinity of Houston using a fully coupled meteorology-chemistry-aerosol model, *J. Geophys. Res.-Atmos.*, 111, D21305, doi:10.1029/2005jd006721, 2006.
- Finlayson-Pitts, B. J., and Pitts, J. N.: Chemistry of the upper and lower atmosphere: Theory, experiments and applications, Academic Press, San Diego, CA, USA, xxii, 969 pp., 1999.
- Fischer, M. L. and Littlejohn D.: Ammonia at Blodgett Forest, Sierra Nevada, USA, *Atmos. Chem. Phys. Discuss.*, 7, 14 139–14 169, 2007, <http://www.atmos-chem-phys-discuss.net/7/14139/2007/>.
- Fisseha, R., Dommen, J., Gaeggeler, K., Weingartner, E., Sam-burova, V., Kalberer, M., and Baltensperger, U.: Online gas and aerosol measurement of water soluble carboxylic acids in zurich, *J. Geophys. Res.-Atmos.*, 111, D12316, doi:10.1029/2005JD006782, 2006.
- Fortner, E. C., Zhao, J., and Zhang, R. Y.: Development of ion drift-chemical ionization mass spectrometry, *Anal. Chem.*, 76, 5436–5440, 2004.
- Fountoukis, C., Nenes, A., Sullivan, A., Weber, R., VanReken, T., Fischer, M., Matías, E., Moya, M., Farmer, D., and Cohen, R. C.: Thermodynamic characterization of Mexico City aerosol during MILAGRO 2006, *Atmos. Chem. Phys. Discuss.*, 7, 9203–9233, 2007, <http://www.atmos-chem-phys-discuss.net/7/9203/2007/>.
- Furutani, H. and Akimoto, H.: Development and characterization of a fast measurement system for gas-phase nitric acid with a chemical ionization mass spectrometer in the marine boundary layer, *J. Geophys. Res.-Atmos.*, 107, 4016, doi:10.1029/2000JD000269, 2002.
- Geyer, A. and Stutz, J.: Vertical profiles of NO<sub>3</sub>, N<sub>2</sub>O<sub>5</sub>, O<sub>3</sub>, and NO<sub>x</sub> in the nocturnal boundary layer: 2. Model studies on the altitude dependence of composition and chemistry, *J. Geophys. Res.-Atmos.*, 109, D12307, doi:10.1029/2004JD005217, 2004.
- Hering, S. V., Lawson, D. R., Allegrini, I., Febo, A., Perrino, C., Possanzini, M., Sickles, J. E., Anlauf, K. G., Wiebe, A., Appel, B. R., John, W., Ondo, J., Wall, S., Braman, R. S., Sutton, R., Cass, G. R., Solomon, P. A., Eatough, D. J., Eatough, N. L., Ellis, E. C., Grosjean, D., Hicks, B. B., Womack, J. D., Horrocks, J., Knapp, K. T., Ellestad, T. G., Paur, R. J., Mitchell, W. J., Pleasant, M., Peake, E., Maclean, A., Pierson, W. R., Brachaczek, W., Schiff, H. I., Mackay, G. I., Spicer, C. W., Stedman, D. H., Winer, A. M., Biermann, H. W., and Tuazon, E. C.: The nitric-acid shootout – field comparison of measurement methods, *Atmos. Environ.*, 22, 1519–1539, 1988.
- Hodzic, A., Flocke, F. M., Madronich, S., Fast, J., Zheng, W., Weinheimer, A., Montzka, D., Knapp, D., Mauldin, L., Wennberg, P., Crounse, J. D., McCabe, D., Clarke, A., Hostetler, C. A., and Hair, J. W.: Contribution of dust particles to the heterogeneous removal of acidic gases from the atmosphere during the MIRAGE experiment, *Eos Trans. AGU*, 88(52), Fall Meet. Suppl., Abstract A23C-1476, 2007.
- Horii, C. V., Munger, J. W., Wofsy, S. C., Zahniser, M., Nelson, D., and McManus, J. B.: Atmospheric reactive nitrogen concentration and flux budgets at a Northeastern US forest site, *Agr. Forest Meteorol.*, 136, 159–174, 2006.
- Huey, L. G., Hanson, D. R., and Howard, C. J.: Reactions of SF<sub>6</sub><sup>-</sup> and I<sup>-</sup> with atmospheric trace gases, *J. Phys. Chem.*, 99, 5001–5008, 1995.
- Huey, L. G. and Lovejoy, E. R.: Reactions of SiF<sub>5</sub><sup>-</sup> with atmospheric trace gases: Ion chemistry for chemical ionization detection of HNO<sub>3</sub> in the troposphere, *Int. J. Mass Spectrom.*, 155, 133–140, 1996.
- Huey, L. G., Dunlea, E. J., Lovejoy, E. R., Hanson, D. R., Norton, R. B., Fehsenfeld, F. C., and Howard, C. J.: Fast time response measurements of HNO<sub>3</sub> in air with a chemical ionization mass spectrometer, *J. Geophys. Res.-Atmos.*, 103, 3355–3360, 1998.
- Huey, L. G., Tanner, D. J., Slusher, D. L., Dibb, J. E., Arimoto, R., Chen, G., Davis, D., Buhr, M. P., Nowak, J. B., Mauldin, R. L., Eisele, F. L., and Kosciuch, E.: CIMS measurements of HNO<sub>3</sub> and SO<sub>2</sub> at the south pole during ISCAT 2000, *Atmos. Environ.*, 38, 5411–5421, 2004.
- Huey, L. G.: Measurement of trace atmospheric species by chemical ionization mass spectrometry: Speciation of reactive nitrogen and future directions, *Mass Spectrom. Rev.*, 26, 166–184, 2007.
- JPL 06-2: Chemical Kinetics and Photochemical Data for Use in Atmospheric Studies Evaluation Number 15, National Aeronautics and Space Administration, Jet Propulsion Laboratory, California Institute of Technology, Pasadena, CA, USA, 2006.
- Kajino, M., Ueda, H., and Nakayama, S.: Secondary acidification: Changes in gas-aerosol partitioning of semivolatile nitric acid and enhancement of its deposition due to increased emission and concentration of SO<sub>x</sub>, *J. Geophys. Res.*, 113, D03302, doi:10.1029/2007JD008635, 2008.
- Karagulian, F., and Rossi, M. J.: Heterogeneous chemistry of the no<sub>3</sub> free radical and n<sub>2</sub>o<sub>5</sub> on decane flame soot at ambient temperature: Reaction products and kinetics, *J. Phys. Chem. A*, 111, 1914–1926, 2007.
- Lei, W., de Foy, B., Zavala, M., Volkamer, R., and Molina, L. T.: Characterizing ozone production in the Mexico City metropolitan area: A case study using a chemical transport model, *Atmos. Chem. Phys.*, 7, 1347–1366, 2007, <http://www.atmos-chem-phys.net/7/1347/2007/>.
- Lei, W., Zhang, R., McGivern, W. S., Derecskei-Kovacs, A., and North, S. W.: Theoretical study of isomeric branching in the isoprene-OH reaction: Implications to final product yields in Isoprene Oxidation, *Chem. Phys. Lett.*, 326, 109–114, 2000.
- Lei, W. F., Zhang, R. Y., Tie, X. X., and Hess, P.: Chemical charac-

- terization of ozone formation in the Houston-Galveston area: A chemical transport model study, *J. Geophys. Res.-Atmos.*, 109, D12301, doi:10.1029/2003JD004219, 2004.
- Maring, H., Savoie, D. L., Izaguirre, M. A., Custals, L., and Reid, J. S.: Mineral dust aerosol size distribution change during atmospheric transport, *J. Geophys. Res.-Atmos.*, 108(D19), 8592, doi:10.1029/2002JD002536, 2003.
- Mason, E. A. and McDaniel, E. W.: Transport properties of ions in gases, Wiley, New York, USA, xvi, 560 pp., 1988.
- Molina, L. T. and Molina, M. J.: Air quality in the Mexico megacity: An integrated assessment, Alliance for global sustainability book series, 2, Kluwer Academic Publishers, Dordrecht, The Netherlands, Boston, USA, xxi, 384 pp., 2002.
- Molina, M. J. and Molina, L. T.: Megacities and atmospheric pollution, *J. Air Waste Ma.*, 54, 644–680, 2004.
- Molina, L. T., Kolb, C. E., de Foy, B., Lamb, B. K., Brune, W. H., Jimenez, J. L., Ramos-Villegas, R., Sarmiento, J., Paramo-Figueroa, V. H., Cardenas, B., Gutierrez-Avedoy, V., and Molina, M. J.: Air quality in north America's most populous city – overview of the MCMA-2003 campaign, *Atmos. Chem. Phys.*, 7, 2447–2473, 2007, <http://www.atmos-chem-phys.net/7/2447/2007/>.
- Molina, L. T., Madronich, S., Gaffney, J. S., Singh, H. B.: Overview of MILAGRO/INTEX-B Campaign, *IGAC Newsletter*, Issue No. 38, 2–15, April 2008.
- Moya, M., Grutter, M., and Baez, A.: Diurnal variability of size-differentiated inorganic aerosols and their gas-phase precursors during January and February of 2003 near downtown Mexico City, *Atmos. Environ.*, 38, 5651–5661, 2004.
- Myles, L., Meyers, T. P., and Robinson, L.: Relaxed eddy accumulation measurements of ammonia, nitric acid, sulfur dioxide and particulate sulfate dry deposition near Tampa, FL, USA, *Environ. Res. Lett.*, 2, 034004, doi:10.1088/1748-9326/2/3/034004, 2007.
- Neuman, J. A., Huey, L. G., Ryerson, T. B., and Fahey, D. W.: Study of inlet materials for sampling atmospheric nitric acid, *Environ. Sci. Technol.*, 33, 1133–1136, 1999.
- Okumura, M. and Sander, S. P.: Gas-Phase Formation Rates of Nitric Acid and its Isomers under Urban Conditions – Final Report to California Air Resources Board, CARB Contract No. 03-333, 21 November 2005.
- Perrino, C., Desantis, F., and Febo, A.: Criteria for the choice of a denuder sampling technique devoted to the measurement of atmospheric nitrous and nitric-acids, *Atmos. Environ. a-Gen.*, 24, 617–626, 1990.
- Pryor, S. C. and Klemm, O.: Experimentally derived estimates of nitric acid dry deposition velocity and viscous sub-layer resistance at a conifer forest. *Atmos. Environ.*, 38, 2769–2777, 2004.
- Querol, X., Pey, J., Minguillón, M. C., Pérez, N., Alastuey, A., Viana, M., Moreno, T., Bernabé, R. M., Blanco, S., Cárdenas, B., Vega, E., Sosa, G., Escalona, S., Ruiz, H., and Artíñano, B.: PM speciation and sources in Mexico during the MILAGRO-2006 Campaign, *Atmos. Chem. Phys.*, 8, 111–128, 2008, <http://www.atmos-chem-phys.net/8/111/2008/>.
- Ramazan, K. A., Wingen, L. M., Miller, Y., Chaban, G. M., Gerber, R. B., Xanthreas, S. S., and Finlayson-Pitts, B. J.: New experimental and theoretical approach to the heterogeneous hydrolysis of  $\text{NO}_2$ : Key role of molecular nitric acid and its complexes, *J. Phys. Chem. A*, 110, 6886–6897, doi:10.1021/Jp056426n, 2006.
- Salcedo, D., Onasch, T. B., Dzepina, K., Canagaratna, M. R., Zhang, Q., Huffman, J. A., DeCarlo, P. F., Jayne, J. T., Mortimer, P., Worsnop, D. R., Kolb, C. E., Johnson, K. S., Zuberi, B., Marr, L. C., Volkamer, R., Molina, L. T., Molina, M. J., Cardenas, B., Bernabe, R. M., Marquez, C., Gaffney, J. S., Marley, N. A., Laskin, A., Shutthanandan, V., Xie, Y., Brune, W., Lesher, R., Shirley, T., and Jimenez, J. L.: Characterization of ambient aerosols in Mexico City during the MCMA-2003 campaign with aerosol mass spectrometry: Results from the CENICA supersite, *Atmos. Chem. Phys.*, 6, 925–946, 2006, <http://www.atmos-chem-phys.net/6/925/2006/>.
- Saliba, N. A., Yang, H., and Finlayson-Pitts, B. J.: Reaction of gaseous nitric oxide with nitric acid on silica surfaces in the presence of water at room temperature, *J. Phys. Chem. A*, 105, 10 339–10 346, doi:10.1021/Jp012330r, 2001.
- Seinfeld, J. H. and Pandis, S. N.: *Atmospheric Chemistry and Physics: From Air Pollution to Climate Change*, Wiley, New York, USA, xxvii, 1326 pp., 1998.
- Sillman, S.: The relation between ozone, nox and hydrocarbons in urban and polluted rural environments, *Atmos. Environ.*, 33, 1821–1845, 1999.
- Simon, P. K. and Dasgupta, P. K.: Continuous automated measurement of gaseous nitrous and nitric-acids and particulate nitrite and nitrate, *Environ. Sci. Technol.*, 29, 1534–1541, 1995.
- Slusher, D. L., Huey, L. G., Tanner, D. J., Flocke, F. M., and Roberts, J. M.: A thermal dissociation-chemical ionization mass spectrometry (TD-CIMS) technique for the simultaneous measurement of peroxyacetyl nitrates and dinitrogen pentoxide, *J. Geophys. Res.-Atmos.*, 109, D19315, 2004.
- Stutz, J., Alicke, B., Ackermann, R., Geyer, A., White, A., and Williams, E.: Vertical profiles of  $\text{NO}_3$ ,  $\text{N}_2\text{O}_5$ ,  $\text{O}_3$ , and  $\text{NO}_x$  in the nocturnal boundary layer: 1. Observations during the Texas air quality study 2000, *J. Geophys. Res.-Atmos.*, 109, D12306, doi:10.1029/2003JD004209, 2004.
- Suh, I., Lei, W. F., and Zhang, R. Y.: Experimental and theoretical studies of isoprene reaction with  $\text{NO}_3$ , *J. Phys. Chem. A*, 105, 6471–6478, 2001.
- Suh, I., Zhang, D., Zhang, R., Molina, L. T., and Molina, M. J.: Theoretical study of OH addition to toluene, *Chem. Phys. Lett.*, 364, 454–462, 2002.
- Suh, I., Zhang, R., Molina, L. T., and Molina, M. J.: Oxidation mechanism of aromatic peroxy and bicyclic radicals from OH-toluene reactions, *J. Am. Chem. Soc.*, 125, 12 655–12 665, 2003.
- Talbot, R. W., Vijgen, A. S., and Harriss, R. C.: Measuring tropospheric  $\text{HNO}_3$  – problems and prospects for nylon filter and mist chamber techniques, *J. Geophys. Res.-Atmos.*, 95, 7553–7561, 1990.
- Tie, X., Zhang, R., Brasseur, G., Emmons, L., and Lei, W.: Effects of lightning on reactive nitrogen and nitrogen reservoir species, *J. Geophys. Res.*, 106, 3167–3178, 2001.
- Tie, X. X., Madronich, S., Li, G. H., Ying, Z. M., Zhang, R., Garcia, A. R., Lee-Taylor, J., and Liu, Y. B.: Characterizations of chemical oxidants in Mexico City: A regional chemical dynamical model (WRF-CHEM) study, *Atmos. Environ.*, 41, 1989–2008, 2007.
- Viehland, L. A., Mason, E. A., Morrison, W. F., and Flannery, M. R.: Tables of transport collision integrals for (n, 6, 4) ion-neutral potentials, *Atom Data Nucl Data*, 16, 495–514, 1975.
- Volkamer, R., Jimenez, J. L., San Martini, F., Dzepina, K., Zhang, Q., Salcedo, D., Molina, L. T., Worsnop, D. R., and Molina, M.

- J.: Secondary Organic Aerosol Formation from Anthropogenic Air Pollution: Rapid and Higher than Expected, *Geophys. Res. Lett.*, 33(17), L17811, doi:10.1029/2006GL026899, 2006.
- Volkamer, R., Sheehy, P. M., Molina, L. T., and Molina, M. J.: Oxidative capacity of the Mexico City atmosphere – Part 1: A radical source perspective, *Atmos. Chem. Phys. Discuss.*, 7, 5365–5412, 2007, <http://www.atmos-chem-phys-discuss.net/7/5365/2007/>.
- Zhang, D., Zhang, R., Park, J., and North, S. W.: Hydroxy peroxy nitrates and nitrates from OH initiated reactions of isoprene, *J. Am. Chem. Soc.*, 124, 9600–9605, 2002.
- Zhang, R., Leu, M. T., and Keyser, L. F.: Hydrolysis of  $\text{N}_2\text{O}_5$  and  $\text{ClONO}_2$  on the  $\text{H}_2\text{SO}_4/\text{HNO}_3/\text{H}_2\text{O}$  ternary solutions under stratospheric conditions, *Geophys. Res. Lett.*, 22, 1493–1496, 1995.
- Zhang, R., Tie, X., and Bond, D. W.: Impacts of anthropogenic and natural  $\text{NO}_x$  sources over the US on tropospheric chemistry, *P. Natl. Acad. Sci. USA*, 100, 1505–1509, 2003.
- Zhang, R. Y., Lei, W. F., Tie, X. X., and Hess, P.: Industrial emissions cause extreme urban ozone diurnal variability, *P. Natl. Acad. Sci. USA*, 101, 6346–6350, 2004a.
- Zhang, R. Y., Suh, I., Zhao, J., Zhang, D., Fortner, E. C., Tie, X. X., Molina, L. T., and Molina, M. J.: Atmospheric new particle formation enhanced by organic acids, *Science*, 304, 1487–1490, 2004b.
- Zhao, J. and Zhang, R. Y.: Proton transfer reaction rate constants between hydronium ion ( $\text{H}_3\text{O}^{(+)}$ ) and volatile organic compounds, *Atmos. Environ.*, 38, 2177–2185, 2004a.
- Zhao, J., Zhang, R., Fortner, E. C., and North, S. W.: Quantification of hydroxycarbonyls from OH-isoprene reactions, *J. Am. Chem. Soc.*, 126, 2686–2687, 2004b.